Available online at www.sciencedirect.com
SCIENCE DIRECT
Journal of Computational Physics 216 (2006) 637–653
JOURNAL OF COMPUTATIONAL PHYSICS
www.elsevier.com/locate/jcp

Optimal grid-based methods for thin film micromagnetics simulations

C.B. Muratov [a,*], V.V. Osipov [b]

[a] Department of Mathematical Sciences, New Jersey Institute of Technology, University Heights, Newark, NJ 07102, United States
[b] Mission Critical Technologies, Inc., 2041 Rosecrans Avenue, Suite 225, El Segundo, CA 90245, United States

Received 31 August 2005; received in revised form 19 December 2005; accepted 30 December 2005
Available online 24 February 2006

Abstract

Thin film micromagnetics are a broad class of materials with many technological applications, primarily in magnetic memory. The dynamics of the magnetization distribution in these materials is traditionally modeled by the Landau–Lifshitz–Gilbert (LLG) equation. Numerical simulations of the LLG equation are complicated by the need to compute the stray field due to the inhomogeneities in the magnetization which presents the chief bottleneck for the simulation speed. Here, we introduce a new method for computing the stray field in a sample for a reduced model of ultra-thin film micromagnetics. The method uses a recently proposed idea of optimal finite difference grids for approximating Neumann-to-Dirichlet maps and has an advantage of being able to use non-uniform discretization in the film plane, as well as an efficient way of dealing with the boundary conditions at infinity for the stray field. We present several examples of the method's implementation and give a detailed comparison of its performance for studying domain wall structures compared to the conventional FFT-based methods.

Keywords: Micromagnetics; Domain walls; Stray field; Optimal grids; Rational approximations

1. Introduction

Domain structures determine many properties of real magnetic materials and memory systems, and are a ubiquitous manifestation of micromagnetism [1–3]. Of particular interest are these structures in thin magnetic metal films [4–8] which have been intensely investigated during the last two decades, primarily because of their giant magnetoresistance [9–13]. They also play an important role in multilayer magnetic-normal metal structures for current-induced reversal of magnetization in a magnetic layer under the action of spin-polarized current [14–16].

The starting point in the study of micromagnetics is the Landau–Lifshitz–Gilbert (LLG) equation, which describes the dynamics of the magnetization vector $\mathbf{M} = (M_1, M_2, M_3)$ of fixed magnitude $|\mathbf{M}| = M_s$ in the material, with Neumann boundary condition [1]:

* Corresponding author. Tel.: +1 973 596 5833; fax: +1 973 596 5591.
E-mail address: muratov@njit.edu (C.B. Muratov).

0021-9991/$ - see front matter © 2006 Elsevier Inc. All rights reserved.
doi:10.1016/j.jcp.2005.12.018

$$\frac{\partial \mathbf{M}}{\partial t} = -\frac{g|e|}{2mc}\left(\mathbf{M}\times\mathbf{H}_{\text{eff}} + \frac{\alpha}{M_s}\mathbf{M}\times\mathbf{M}\times\mathbf{H}_{\text{eff}}\right), \quad v\cdot\nabla\mathbf{M}|_{\partial\Omega} = 0. \tag{1}$$

Here, $\mathbf{M} = \mathbf{M}(\mathbf{r}, t)$, with $\mathbf{r} = (x, y, z) \in \Omega \subset \mathbb{R}^3$, where Ω is the domain occupied by the material; $\gamma = g|e|/(2mc)$ is the gyromagnetic ratio (we are using the CGS units here), and α is a dimensionless parameter. The first term in (1) governs the precession of the magnetization vector in the presence of the effective magnetic field $\mathbf{H}_{\text{eff}}$, and the second term introduces phenomenological damping. The effective field $\mathbf{H}_{\text{eff}}$ is determined self-consistently as

$$\mathbf{H}_{\text{eff}} = -\frac{\delta E}{\delta \mathbf{M}}, \tag{2}$$

where the energy functional $E[\mathbf{M}]$ is given by

$$E[\mathbf{M}] = \int_\Omega \left(-\frac{K}{2M_s^2}M_2^2 + \frac{A}{2M_s^2}|\nabla\mathbf{M}|^2 - \mathbf{H}\cdot\mathbf{M}\right)\mathrm{d}^3\mathbf{r} + \frac{1}{2}\int_{\mathbb{R}^3}\int_{\mathbb{R}^3}\frac{\nabla\cdot\mathbf{M}(\mathbf{r})\nabla\cdot\mathbf{M}(\mathbf{r}')}{|\mathbf{r}-\mathbf{r}'|}\mathrm{d}^3\mathbf{r}\,\mathrm{d}^3\mathbf{r}'. \tag{3}$$

This energy consists of the anisotropy (first term), exchange (second term), external field (third term), and the magnetostatic (fourth term) contributions, with K and A being the respective material constants, and $\mathbf{H}$ the applied field. Note that we assumed the material to be uniaxial, with the x_2-axis as the direction of the easy axis. Also note that the last term in (3) should be understood in the distributional sense by extending $\mathbf{M}$ to $\mathbf{M} = 0$ outside of Ω to take into account surface "charges" on $\partial\Omega$.

It has long been realized that the LLG equation is a paradigm for multiscale modeling (for a review, see [17]). Even the study of equilibrium properties of magnetic materials require dealing with an intricate energy landscape associated with issues of non-locality, non-convexity, and the hard constraint $|\mathbf{M}| = \text{const.}$, apart from the need to consider, in general, complex three-dimensional geometries. For the time-dependent problem, a further complication arises from the general need to resolve fast wave-like dynamics due to spin precession (magnons) and the slow dissipative time scales.

Therefore, direct numerical simulations of (1)–(3) would certainly be impractical without giving special consideration to the type of material, geometry, and experimental protocol involved in a particular setting. These considerations can also guide the introduction of various approximations which can make the obtained reduced models more amenable to computational studies [18–20]. Specifically, one important class of problems in modeling magnetic materials has to do with thin film uniaxial ferromagnets with the easy axis in the film plane. These materials have been the subject of intense analytical and computational studies in recent years (see, e.g., [21–29]). Recently, efficient numerical approaches for dealing with the constraint $|\mathbf{M}| = \text{const.}$, using unconditionally stable time-stepping procedure were developed [30]. Still, the main bottleneck in the numerical solution of (1) is the calculation of the magnetostatic contribution to the effective field (the "stray field").

One approach to stray field computation in the context of thin film micromagnetics has traditionally been to use fast Fourier transform (FFT) to evaluate the discrete versions of the integrals with the Newtonian potential giving rise to the last term in (3) [25]. In such an approach the evaluation of the stray field is quite efficient. The price to pay, however, is that the computational domain must be discretized on a uniform rectangular lattice. Apart from the need to account for boundary effects [28], this approach has limitations in dealing with disparate length scales that are inherent in thin film micromagnetics problems. Alternatively, one could compute the stray field by discretizing the equation of magnetostatics in the whole of $\mathbb{R}^3$. However, this approach has the need for the boundary condition at the boundary of three-dimensional computational domain, a common difficulty for the numerical studies of exterior problems [31].

The purpose of this paper is to develop an alternative approach to evaluating the stray field in thin film micromagnetics problems, which possesses both the efficiency of the FFT techniques and can deal with non-uniform grids. In contrast to previous studies, we are going to use a recently proposed idea of optimal finite difference grids for approximating Neumann-to-Dirichlet maps arising from the solutions of elliptic boundary value problems [32–34]. Thin film micromagnetics problems are ideally suited for that, as the stray field is directly related to the Neumann-to-Dirichlet operator for the Laplace's equation in half-space. We will demonstrate the efficiency of these methods by studying domain wall structures in one- and two-dimensional ferromagnetic films in a reduced model of thin film micromagnetics that is applicable to a wide range of materials [19].

Our paper is organized as follows. In Section 2, we introduce a reduced model that is appropriate for soft ultra-thin film micromagnetics with in-plane easy axis. In Section 3, we review the main ideas of the optimal

grid method and give details of our way of optimal grid construction. In Section 4, we present the results of our numerical analysis for various one- and two-dimensional magnetic domain structures and compare them with the results obtained by conventional methods. Finally, we summarize in Section 5.

2. Reduced model for thin film micromagnetics

First let us introduce a simplified version of the LLG equation in the case of ultra-thin film micromagnetics, which will be easier and more transparent for our treatment of the magnetostatic energy and eliminates the need to deal with other unrelated numerical issues associated with the LLG equation. Our approach here is very similar to the reduction introduced by Garcia-Cervera and E [19].

Assume that $\Omega = D \times [0, d]$, with d small (we will later specify what that means), that is, Ω is a thin layer with the base $D \subseteq \mathbb{R}^2$. Introducing

$$\mathbf{m} = \frac{\mathbf{M}}{M_s}, \quad \mathbf{h} = \frac{M_s \mathbf{H}}{K}, \tag{4}$$

so that $|\mathbf{m}| = 1$ in Ω, and rescaling

$$\mathbf{r} \to \mathbf{r}\sqrt{\frac{A}{K}}, \quad t \to t\frac{2mcM_s}{g|e|K}, \tag{5}$$

we write (1) to the leading order in d as

$$\frac{\partial \mathbf{m}}{\partial t} = -\mathbf{m} \times \mathbf{h}_{\text{eff}} - \alpha \mathbf{m} \times \mathbf{m} \times \mathbf{h}_{\text{eff}}, \tag{6}$$

$$\mathbf{h}_{\text{eff}} = m_2 \mathbf{e}_2 + \Delta \mathbf{m} + \mathbf{h} - \frac{1}{Q} m_3 \mathbf{e}_3 + \frac{v}{4\pi} \nabla \int_{\mathbb{R}} \frac{\nabla \cdot \mathbf{m}(\mathbf{r}')}{|\mathbf{r} - \mathbf{r}'|} \mathrm{d}^2 \mathbf{r}', \tag{7}$$

where now $\mathbf{r} \in D \subseteq \mathbb{R}^2$, and we introduced two dimensionless parameters:

$$Q = \frac{K}{4\pi M_s^2}, \quad v = \frac{4\pi M_s^2 d}{\sqrt{AK}}. \tag{8}$$

The first parameter, Q, is the quality factor that measures the relative strength of the magnetostatic and anisotropy energies in the bulk material, this is typically a small parameter ranging from $Q \simeq 0.1$ for materials like cobalt alloys, to $Q \simeq 2.5 \times 10^{-4}$ for very soft magnetic materials like permalloy [1,35]. The second parameter, v, measures the relative strength of the magnetostatics in thin film, it can be both small and large depending on the material and the film thickness.

It is easier to understand the meaning of the approximation introduced in terms of the two lengths: the exchange length $l = (A/4\pi M_s^2)^{1/2}$ and the Bloch wall thickness $L = (A/K)^{1/2}$, then $Q = (l/L)^2$. For example, in cobalt alloys $l \simeq 5$ nm, and for a material with $Q = 0.1$ we will have $L \simeq 15$ nm. The thin film approximation is justified, if the thickness of the film does not exceed the exchange length: $d \lesssim l$ (more precisely, when $d \lesssim 7l$ in the context of Neel walls) [1,35,27]. On the other hand, in terms of l and L we have $v = Ld/l^2$, and so for an ultra-thin cobalt alloy film above with $d = 2$ nm we get $v \simeq 1$. Alternatively, in permalloy with $Q = 2.5 \times 10^{-4}$ we have $l \simeq 5$ nm and $L \simeq 316$ nm [29], and so for a film of $d = 20$ nm thickness we get $v \simeq 250$.

We now make a crucial observation that the last term in (7) is a gradient of potential φ which is essentially the Neumann-to-Dirichlet map associated with the Laplace's equation in the half-space applied to the magnetic charge density $-\nabla \cdot \mathbf{m}$ (see Section 3.1):

$$\varphi = -\frac{1}{2}(-\Delta)^{-1/2} \nabla \cdot \mathbf{m}, \quad (-\Delta)^{-1/2} v(\mathbf{r}) = \frac{1}{2\pi} \int_{\mathbb{R}^2} \frac{v(\mathbf{r}')}{|\mathbf{r} - \mathbf{r}'|} \mathrm{d}^2 \mathbf{r}'. \tag{9}$$

Thus, obtaining the contribution of the magnetostatic energy to the effective field $\mathbf{h}_{\text{eff}}$ reduces to accurately evaluating this Neumann-to-Dirichlet map. This will be the main point of our computational approach below.

In the following, we are going to consider the situation in which $Q \ll 1$ and $\mathbf{h} = (0, h, 0)$, which is relevant to the problem of magnetic switching, while assuming that both anisotropy, exchange, and the magnetostatics remain significant. This essentially implies that we consider the limit $Q \to 0$ and $v = \mathrm{O}(1)$, which can be achieved

by passing to the limit $K \to 0$ and $d = \mathrm{O}(K^2)$ in the LLG equation. This then allows a further simplification of (6), since for $Q \ll 1$ the out-of-plane magnetization component m_3 is strongly penalized. Assuming that $\mathbf{m} \simeq (m_1, m_2, 0)$ and retracing the arguments of [19], we then find that the first two components $\tilde{\mathbf{m}} = (m_1, m_2)$ of the magnetization vector $\mathbf{m}$ solve (see also [23])

$$\frac{\partial \tilde{\mathbf{m}}}{\partial t} = -\left(\alpha + \frac{1}{\alpha}\right) \tilde{\mathbf{m}} \times \tilde{\mathbf{m}} \times \tilde{\mathbf{h}}_{\mathrm{eff}}, \tag{10}$$

where $\tilde{\mathbf{h}}_{\mathrm{eff}}$ is the in-plane component of $\mathbf{h}_{\mathrm{eff}}$. Interestingly, the obtained effective equation is the overdamped version of the original LLG equation, with the Gilbert constant α replaced by $\alpha + \alpha^{-1}$. Since in most materials $\alpha \ll 1$, this has an effect of effectively increasing the rate of dissipation by a large factor and eliminates the need to track spin precession [19,23]. The consistency criterion for the validity of this equation is $Q \ll \alpha$, which is satisfied in soft materials, since typically $\alpha \sim 0.01$ [1].

This equation can be conveniently written in terms of the angle θ between $\tilde{\mathbf{m}}$ and the easy axis. Setting $\tilde{\mathbf{m}} = (-\sin\theta, \cos\theta)$, we obtain

$$\frac{\partial \theta}{\partial t} = \Delta\theta - \frac{1}{2}\sin 2\theta - h\sin\theta + v\cos\theta\frac{\partial \varphi}{\partial x} + v\sin\theta\frac{\partial \varphi}{\partial y}, \tag{11}$$

$$\varphi = \frac{1}{2}(-\Delta)^{-1/2}\left(\cos\theta\frac{\partial \theta}{\partial x} + \sin\theta\frac{\partial \theta}{\partial y}\right) + \text{surface terms}, \tag{12}$$

where we absorbed the factor of $\alpha + \alpha^{-1}$ into the definition of time.

3. Optimal grid-based discretization

Our approach to the problem of evaluating the magnetostatic potential φ uses the recently proposed concept of optimal grids for accurate approximation of the Neumann-to-Dirichlet operator for elliptic boundary value problems [32–34]. We will first recall the basic ideas of the optimal grid method and then apply it to the problem of thin film micromagnetics.

3.1. Neumann-to-Dirichlet map for the Laplace's equation in half-space

Let us briefly recall the definition of the Neumann-to-Dirichlet operator $\mathcal{N}$ for the Laplace's equation in $\mathbb{R}^3$ with the boundary data prescribed on the plane $z = 0$. Let u solve

$$\Delta u + \frac{\partial^2 u}{\partial z^2} = 0, \quad z > 0, \tag{13}$$

where $\Delta = \partial^2/\partial x^2 + \partial^2/\partial y^2$ is the Laplacian in the plane, as in (12), with either Dirichlet

$$u(x, y, 0) = \varphi(x, y) \tag{14}$$

or Neumann boundary conditions

$$\lim_{z \to 0^+} \frac{\partial u(x, y, z)}{\partial z} = -v(x, y). \tag{15}$$

For appropriately chosen boundary data φ or v this boundary value problem has a unique solution. Furthermore, there is a one-to-one correspondence between v and φ via the Neumann-to-Dirichlet operator [36]

$$\varphi = \mathcal{N} v. \tag{16}$$

For the considered problem, it can be computed in closed form. Fourier-transforming (13) in x and y, we obtain

$$\frac{\mathrm{d}^2 u_{\mathbf{q}}}{\mathrm{d}z^2} = |\mathbf{q}|^2 u_{\mathbf{q}}, \quad u_{\mathbf{q}}(0) = \varphi_{\mathbf{q}}, \quad \varphi_{\mathbf{q}} = \int_{\mathbb{R}^2} \mathrm{e}^{\mathrm{i}\mathbf{q}\cdot\mathbf{r}} \varphi(\mathbf{r})\, \mathrm{d}^2\mathbf{r}, \tag{17}$$

whose bounded solution is $u_{\mathbf{q}}(z) = \varphi_{\mathbf{q}}\, e^{-|\mathbf{q}|z}$. From this, we easily see that $v_{\mathbf{q}} = -\lim_{z\to 0^+} du_{\mathbf{q}}/dz$ is

$$v_{\mathbf{q}} = |\mathbf{q}|\varphi_{\mathbf{q}}. \tag{18}$$

so the Fourier Transform $\mathcal{N}_{\mathbf{q}}$ of $\mathcal{N}$, and the operator $\mathcal{N}$ itself, obtained by inverting the transform of $\mathcal{N}_{\mathbf{q}}$, are

$$\mathcal{N}_{\mathbf{q}} = \frac{1}{|\mathbf{q}|}, \quad \mathcal{N}v = \frac{1}{2\pi}\int_{\mathbb{R}^2} \frac{v(\mathbf{r}')}{|\mathbf{r}-\mathbf{r}'|}\, d^2\mathbf{r}'. \tag{19}$$

Comparing this with (9), we see that $\mathcal{N}$ and the operator $(-\Delta)^{-1/2}$ defined in (12) are identical, and also $\mathcal{N}_{\mathbf{q}} = 1/\sqrt{\lambda_{\mathbf{q}}}$, where $\lambda_{\mathbf{q}} = |\mathbf{q}|^2$ are the eigenvalues of $-\Delta$, thus justifying the notation (for a general discussion of pseudo-differential operators, see e.g. [36]). Of course, this result is expected, since by symmetry the potential in (19) is simply a single layer potential with density $2v$. For our purposes, however, it is important to emphasize the interpretation of $\mathcal{N}$ as the inverse square root of negative Laplacian, which is the basis for the approach below.

3.2. Optimal grids

Now we describe the idea of the optimal grid method. Here, we will present its derivation from a somewhat different point of view than in [33], emphasizing its approximation theory aspect. The starting point of this approach is to introduce a rational approximation to the impedance function $F(\lambda) = 1/\sqrt{\lambda}$ on a spectral interval $\lambda \in [\lambda_{\min}, \lambda_{\max}]$, which can then be used to approximate the Neumann-to-Dirichlet operator in Fourier space. Various alternatives are possible here [32,34]; we, however, will follow [33] to find the *optimal* rational approximation to the impedance function in the sense of uniform relative error. In other words, we will say that $R(\lambda)$ is an optimal rational approximation to $F(\lambda)$, if

$$\max_{\lambda\in[\lambda_{\min},\lambda_{\max}]} |\sqrt{\lambda}R(\lambda) - 1| = \min_{R_{n-1,n}} \max_{\lambda\in[\lambda_{\min},\lambda_{\max}]} |\sqrt{\lambda}R_{n-1,n}(\lambda) - 1|, \tag{20}$$

where $R_{n-1,n}(\lambda)$ are all rational functions of degree $n-1$ by n. The quality of this approximation depends only on the quantity $\kappa = \lambda_{\max}/\lambda_{\min}$, since the spectral interval on which (20) holds can be adjusted by a simple rescaling of λ.

Existence and uniqueness of the optimal rational approximant for the inverse square root follows from standard theory [37,38], and the explicit solution of this problem goes back to Zolotarev (see [33] and references therein). Furthermore, as was shown in [33], the error of the optimal rational approximation decays exponentially fast with the degree n of the rational function $R(\lambda)$, leading to exponential superconvergence. So in reality quite small values of n will be sufficient for adequate accuracy over large spectral intervals. For example, the (nearly) optimal rational approximant with $n = 4$ on the interval of $\lambda \in [1, 10^4]$ is

$$R(\lambda) = \frac{32}{7\left(\lambda + \frac{197}{9}\right)} + \frac{146}{7\left(\lambda + \frac{3655}{8}\right)} + \frac{2929}{16\left(\lambda + \frac{118697}{8}\right)} + \frac{16}{13\left(\lambda + \frac{2}{3}\right)}, \tag{21}$$

where we rewrote $R(\lambda)$ as a sum of poles and rationalized the obtained coefficients. Let us point out that numerically the optimal rational approximant can be obtained by e.g. Remez algorithm [38], without resorting to the explicit Zolotarev solution. The results presented in this paper are obtained in this manner, using Mathematica software.

The relative error of approximating $F(\lambda)$ by $R(\lambda)$ in (21) is shown in Fig. 1. One can see that with only $n = 4$ this error does not exceed 5.5×10^{-3} on the entire spectral interval. In fact, one can push this even further and obtain an approximant within 5% error for $\kappa = 5\times 10^6$, still with only $n = 4$. On the other hand, choosing $n = 6$ allows one to construct an approximant that is still 5% accurate for $\kappa = 10^{10}$, while for $\lambda \in [1, 10^4]$ the optimal approximant is accurate to already 2×10^{-4} with this value of n. Thus, the Zolotarev approximants are very good for representing the impedance function $F(\lambda)$ with reasonable accuracy over spectral intervals that span many orders of magnitude of λ, with minimal computational complexity. Let us also mention that constructing the optimal approximant to $F(\lambda)$ using Remez algorithm is not a compute-intensive job and takes only a few seconds on an average computer.

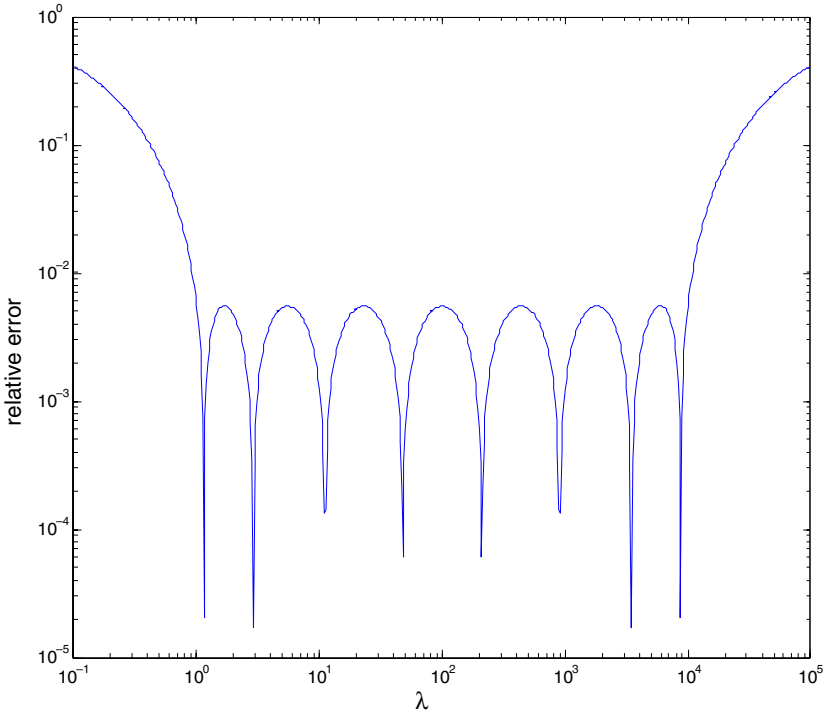

Fig. 1. The relative error of the optimal rational approximation of $1/\sqrt{\lambda}$ on the interval $[1, 10^4]$ with $n = 4$, obtained via Remez algorithm.

The Zolotarev solution implies that one can write

$$R(\lambda) = \sum_{i=1}^{n} \frac{c_i}{\lambda + \lambda_i}, \tag{22}$$

where both $\lambda_i > 0$ and $c_i > 0$ (cf. (21)) [33]. Therefore, up to a transformation $R(\lambda)$ is a Stiltjes function and can be written as a continued fraction (again, up to an equivalence transformation):

$$R(\lambda) = \cfrac{1}{\lambda h_0 + \cfrac{1}{h_{1/2} + \cfrac{1}{\lambda h_1 + \ldots + \cfrac{1}{h_{n-1/2}}}}}, \tag{23}$$

where $h_0, h_{1/2}, h_1, \ldots, h_{n-1/2}$ are all positive [39]. The values of h_i are then obtained from $R(\lambda)$ by a polynomial division algorithm [33]. For example, the values of h_i corresponding to the optimal approximant in (21) are given in Table 1. We note that the accuracy of approximation is not very sensitive to either λ_i, c_i in (22), or the h_i in (23). For example, the coefficients in (21) were determined only up to 10^{-2}. On the other hand, obtaining h_i from λ_i and c_i requires high precision arithmetic and is done better using exact rational arithmetic with rationalized coefficients, as in (21).

What makes this approach work is a remarkable observation by Druskin that (23) is in fact the impedance function for the staggered three-point discretization of (17) with $\lambda = |q|^2$ [32]:

$$\frac{1}{h_i}\left(\frac{u_{i+1} - u_i}{h_{i+1/2}} - \frac{u_i - u_{i-1}}{h_{i-1/2}}\right) - \lambda u_i = 0, \quad i = 0, 1, \ldots n-1, \;\; u_n = 0. \tag{24}$$

Table 1
The values of h_i from (23) corresponding to $R(\lambda)$ in (21)

i	0	1/2	1	3/2	2	5/2	3	7/2
h_i	0.00476822	0.0161362	0.0346346	0.070919	0.147286	0.311252	0.680504	1.71468

More precisely, if we set $(u_0 - u_{-1})/h_{-1/2} = -1$, then it is not difficult to show that $u_0 = R(\lambda)$, where $R(\lambda)$ is given by (23). This suggests to use the following semi-discrete scheme for approximating the Neumann-to-Dirichlet operator $\mathcal{N}$ in (16)

$$\varphi = u_0, \quad v_{-1/2} = -v, \quad u_n = 0, \tag{25}$$

$$u_{i+1} - u_i = h_{i+1/2} v_{i+1/2}, \tag{26}$$

$$v_{i+1/2} - v_{i-1/2} + h_i \Delta u_i = 0, \tag{27}$$

where $i = 0,1,\ldots,n-1$, with $u_i = u_i(x,y)$ and $v_{i+1/2} = v_{i+1/2}(x,y)$ and with the steps h_i obtained from the optimal approximant $R(\lambda)$. In essence, this is a way to approximate the negative square root of the Laplacian, $\mathcal{N} = (-\Delta)^{-1/2}$, in the operator sense. Note that the variables u_i, $v_{i-1/2}$ with $i \geqslant 1$ are purely auxiliary and are not intended to represent the solution of (13) for $z > 0$. Nevertheless, the steps h_i are finely tuned (via the optimal rational approximation procedure) to reproduce the solution of (13) accurately only at $z = 0$ by u_0.

To implement the above scheme in practice, we further discretize the in-plane Laplacian, Δ, using any convenient second-order conservative scheme in the plane and solve the obtained fully discrete problem on a Cartesian product of the two grids. To make the short length scale resolution of both grids consistent, we require that $h_0 = \mathrm{O}(h_\perp)$, where $h_\perp$ is the characteristic size of the grid in the plane. One can easily achieve this by rescaling the step sizes obtained from the rational approximant $R(\lambda)$. The choice of $R(\lambda)$, in turn, is fixed by requiring that $\kappa = \mathrm{O}((L_x^2/h_\perp^2))$, where L_x is the size of the problem in the film plane, and choosing n to achieve the $\mathrm{O}(h_\perp^2)$ accuracy in (20). Note that, alternatively, for a fixed ratio κ a good indicator of the maximum size of the problem for which the Neumann-to-Dirichlet operator is resolved is the total "length"

$$L_z = \sum_{i=0}^{n-1} h_{i+1/2} \tag{28}$$

of the optimal grid.

Quite remarkably, this approach achieves several desirable goals at the same time. First, because of the use of the Zolotarev solution to approximate $(-\Delta)^{-1/2}$, the Neumann-to-Dirichlet operator is approximated *uniformly* in the entire range of wave vectors of the discrete problem. Second, the obtained finite difference scheme is conservative and therefore enjoys all the nice properties of the usual finite difference discretizations of (13), but with vastly fewer nodes in the z-direction. Third, one can use a small stencil in discretizing the Laplacian and therefore find the solution quickly using conjugate gradient (CG) method. This makes the optimal grid method very efficient, as we will show below. But also it is very easy to implement, as the only change from a usual finite difference treatment of the boundary value problem (13) is the special choice of the grid steps in the z-direction. In addition, the possibility to use CG for finding φ makes the algorithm very straightforward to parallelize.

3.3. Optimal geometric grids

Before concluding this section, let us mention that a closed form solution for the step sizes h_i in (23) that become asymptotically equal to Zolotarev steps for large n exists. These are given explicitly by [33]:

$$\begin{aligned} &h_0 = \frac{h_\perp}{1 + \mathrm{e}^{\pi/(2\sqrt{n})}}, \quad h_{1/2} = \mathrm{O}(h_\perp), \\ &h_{i+1/2} = h_{i-1/2}\mathrm{e}^{\pi/\sqrt{n}}, \quad h_i = \sqrt{h_{i+1/2}h_{i-1/2}}. \end{aligned} \tag{29}$$

They correspond to the optimal geometric grids and also give exponential superconvergence in n. However, let us point out that Zolotarev grids require roughly twice fewer nodes to achieve the same accuracy on the same spectral interval. Also, the advantage of Zolotarev grids is that they can achieve a reasonable accuracy of approximating the square root on very large spectral intervals without using too many nodes. On the other hand, optimal geometric grids generally over-resolve the small λ end of the spectral interval when the value of n is increased. Nevertheless, the existence of a simple formula for the steps h_i and reasonably good accuracy for all n make optimal geometric grids a good choice for testing optimal grid codes, or for performing non-demanding computations (for example, in one-dimensional problems).

4. Simulation results

4.1. One-dimensional simulations of Neél walls using optimal geometric grids

We begin by studying the one-dimensional domain wall structures, which are stationary solutions of (11) and (12). Assuming that the domain wall is oriented parallel to the easy axis, we obtain that $\varphi = \varphi(x)$ (for simplicity of notation, we suppress the time dependence of the variables), and so the stray field $h(x)$ is given by

$$h = -\frac{\partial \varphi}{\partial x} = \frac{1}{2}\left(-\frac{\partial^2}{\partial x^2}\right)^{1/2} \sin\theta. \tag{30}$$

Substituting this expression into (11), we find the following evolution equation for the angle variable:

$$\frac{\partial \theta}{\partial t} = \frac{\partial^2 \theta}{\partial x^2} - \frac{1}{2}\sin 2\theta - \frac{v}{2}\cos\theta\left(-\frac{\partial^2}{\partial x^2}\right)^{1/2} \sin\theta. \tag{31}$$

Thus, the evolution of θ is a gradient descent down the non-local energy functional $E[\theta]$ in $L^2(\mathbb{R})$, where

$$E[\theta] = \int_{\mathbb{R}} \left\{\frac{1}{2}\left(\frac{\partial \theta}{\partial x}\right)^2 + \frac{1}{2}\sin^2\theta + \frac{v}{4}\sin\theta\left(-\frac{\partial^2}{\partial x^2}\right)^{1/2} \sin\theta\right\} \mathrm{d}x. \tag{32}$$

Because of the particular geometry chosen, the operator in the last term of (31) is the Dirichlet-to-Neumann map, which can, in turn, be expressed in terms of the bounded solution of the boundary value problem for $u = u(x, z)$ in the upper half-plane:

$$\frac{\partial^2 u}{\partial x^2} + \frac{\partial^2 u}{\partial z^2} = 0, \quad u(x, 0) = \sin\theta(x), \tag{33}$$

$$\left(-\frac{\partial^2}{\partial x^2}\right)^{1/2} \sin\theta(x) = -\left.\frac{\partial u(x, z)}{\partial z}\right|_{z=0^+}. \tag{34}$$

We first write down a semi-discrete version of the problem, slightly modifying the approach of Section 3.2 (see also [33]):

$$u_0(x) = \sin\theta(x), \quad u_n(x) = 0, \tag{35}$$

$$h_i \frac{\mathrm{d}^2 u_i}{\mathrm{d}x^2} + \frac{u_{i+1} - u_i}{h_{i+1/2}} - \frac{u_i - u_{i-1}}{h_{i-1/2}} = 0, \quad i = 1, 2, \ldots, n-1, \tag{36}$$

$$\left(-\frac{\partial^2}{\partial x^2}\right)^{1/2} \sin\theta(x) \approx -\frac{\mathrm{d}^2 u_0}{\mathrm{d}x^2} - \frac{u_1 - u_0}{h_{1/2}}, \tag{37}$$

using geometric optimal grid from (29). We then further discretize the obtained problem in x, using a non-uniform grid $x_j = b\sinh[h_\perp(j - m/2)/b]$, with $j = 0,1, \ldots, m$. This particular discretization is chosen in order to resolve the core of the Neél wall without using fine discretization in the wall tails. To approximate the second derivative at $x = x_j$, we use a staggered grid with arithmetic averaging:

$$\frac{\mathrm{d}^2 u_i}{\mathrm{d}x^2} \approx \frac{1}{x_{j+1/2} - x_{j-1/2}}\left(\frac{u_{i,j+1} - u_{i,j}}{x_{j+1} - x_j} - \frac{u_{i,j} - u_{i,j-1}}{x_j - x_{j-1}}\right), \tag{38}$$

where $u_{i,j} \approx u_i(x_j)$ and $x_{j+1/2} = (x_{j+1} + x_j)/2$. Reflecting boundary conditions are imposed at the boundaries of the computational domain in x.

This discrete problem is then treated as follows. First, for a given set of $\theta_j \approx \theta(x_j)$ we compute the solution $u_{i,j}$ of the discrete boundary value problem using CG with diagonal preconditioner. We then use (37) to compute the approximate Dirichlet-to-Neumann map. After that, we evolve the solution in time using a simple explicit time-stepping scheme (for simplicity of presentation, we do not consider more sophisticated time-stepping techniques here). The solution in the form of the Neél wall is then obtained, starting from a hyperbolic tanh-like profile, as the attained steady-state. An example of the Neél wall solution for $v = 1$ obtained in this manner

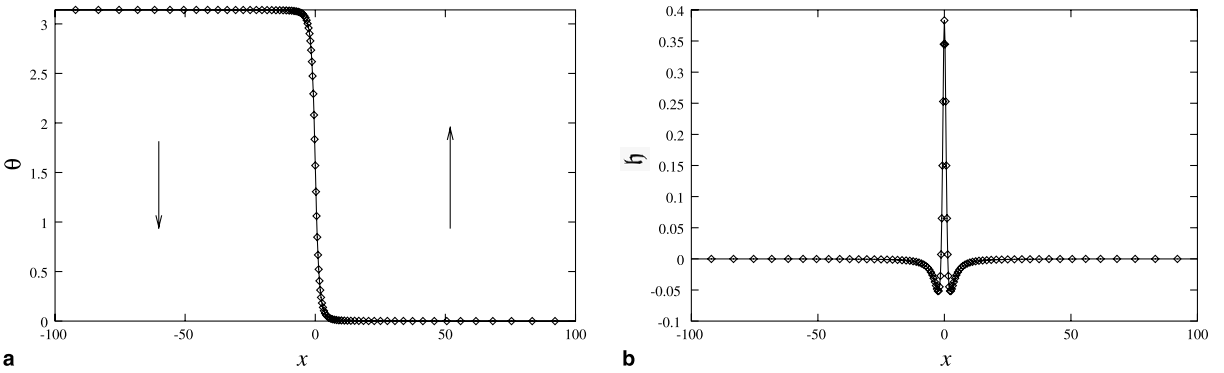

Fig. 2. The profile of the Neél wall at $v = 1$ obtained using optimal geometric grid. Results of the numerical solution of (31) with $h_\perp = 0.25$, $h_{1/2} = 0.125$, $n = 8$, $m = 128$, $b = 3.5$. (a) The angle variable θ (with arrows corresponding to the vector of magnetization away from the wall). (b) The stray field $\hbar$.

is shown in Fig. 2. Here, we used $n = 8$ and $h_{1/2} = h_\perp/2$ for the optimal geometric grid to ensure that all the scales of the discrete problem, down to the shortest scale, are resolved. Let us note that because of the small number of grid points in the direction of the optimal grid the CG iterations are rapidly converging, and the number of iterations needed for convergence decreases with time, as the solution evolves towards steady-state.

Let us now compare the results obtained by this method with the ones obtained using FFT to compute the non-local contributions. We implemented two FFT-based methods: one uses a combination of finite differences with discrete cosine transform to compute the square root of the discrete version of the negative Laplacian (second derivative), and the other is a pseudospectral method. Both are using uniform grids on a sufficiently large finite computational domain.

The results of the comparison of these two methods with those obtained using optimal geometric grids with non-uniform grid in x are presented in Fig. 3. This figure shows the absolute error in the energy of the domain wall for different values of the spatial discretization step size and for different methods as a function of the length of the computational domain (for the purposes of this comparison, the "exact" value of the wall energy was computed using pseudospectral method with small discretization step and on a sufficiently large domain). We find that the optimal geometric grid method requires an order of magnitude less discretization points than

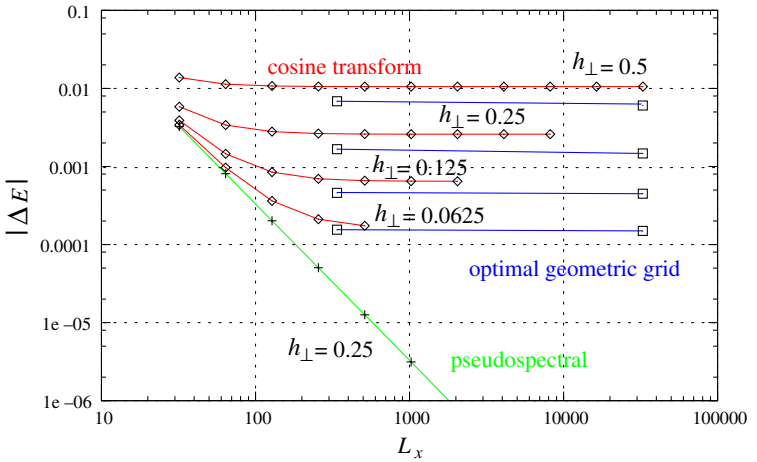

Fig. 3. The absolute error in the energy of the Neél wall with $v = 1$ obtained by different methods. The diamonds correspond to the results of the cosine transform-based simulations (the uniform grid size is given by $h_\perp$). The results of the pseudo spectral method are shown by crosses. The results obtained with the optimal grid method are shown by squares. The optimal geometric grid simulations use $n = 6$ (left square) and $n = 12$ (right square) for each value of $h_\perp$.

the cosine transform method to achieve the same accuracy in the computational domain of the same size. Also, increasing n and m by a factor of 2 (this is the difference between the two squares corresponding to the same value of $h_\perp$ in Fig. 3) puts the method well beyond the resolution limit by the FFT-based methods, as the number of grid points in x for those methods becomes prohibitively large. In fact, choosing the size of the optimal grid (in the z-direction) and that of the non-uniform grid (in the x-direction) to be comparable, we immediately achieve the maximum resolution of the method with a given value of $h_\perp$. This, of course, is very natural and is an attractive feature of the optimal grid methods. Finally, let us note that these results are stable with respect to the choice of $h_{1/2}$. For example, they remain practically unchanged, if instead one uses $n = 6$ and $h_{1/2} = h_\perp$.

4.2. One-dimensional simulations of Neél walls using Zolotarev optimal grids

We now turn to the applications of the optimal grids obtained from the Zolotarev optimal rational approximations of the square root discussed in Section 3.2. Here, we are going to introduce an even more natural discretization scheme that takes into account the physical origin of the non-locality in the magnetostatic energy. This scheme is illustrated in Fig. 4. We represent the film with a series of nodes $x_{j+1/2}$, this is where the magnetization (squares) is defined. To compute the stray field, we need first to evaluate the "charges" (full circles), this is done using centered differences, and the charges are then defined at the midpoints $x_j = (x_{j+1/2} + x_{j-1/2})/2$. The optimal grid, as in Section 3.2, is chosen to be aligned with the charges, as the latter serve as the sources in the discrete elliptic problem:

$$\frac{h_i}{x_{j+1/2} - x_{j-1/2}} \left(\frac{u_{i,j+1} - u_{i,j}}{x_{j+1} - x_j} - \frac{u_{i,j} - u_{i,j-1}}{x_j - x_{j-1}} \right) + \frac{u_{i+1,j} - u_{i,j}}{h_{i+1/2}} - \frac{u_{i,j} - u_{i-1,j}}{h_{i-1/2}} = \frac{1}{2} \left(\frac{\sin\theta_{j+1/2} - \sin\theta_{j-1/2}}{x_{j+1/2} - x_{j-1/2}} \right) \delta_{i,0}, \quad i = 0, 1, \ldots, n-1, \tag{39}$$

where $\delta_{i,j}$ is the Kronecker delta, and we assumed that $u_{-1,j} = u_{0,j}$ and $u_{n,j} = 0$. Note the factor of $\frac{1}{2}$ in the right-hand side of (39), as only half of the total charges contribute to the stray field in the upper half plane (see

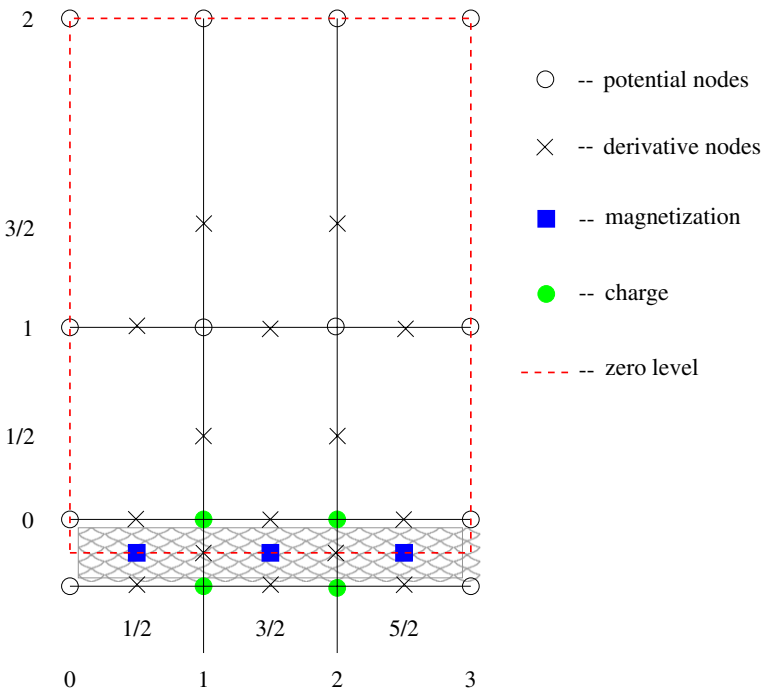

Fig. 4. The schematics of the modified optimal grid-based discretization used in Section 4.2. Here, $m = 3$, $n = 2$.

Fig. 4). Dirichlet boundary conditions are imposed on the boundaries of the computational domain: $u_{i,0} = u_{i,m} = 0$.

Once the solution of the discrete problem is obtained, the values of the magnetostatic potential are available at the nodes x_j. We can then, once again, use centered difference to find the magnetic field (the derivative of the potential) at nodes $x_{j+1/2}$:

$$h_{j+1/2} = -\frac{u_{0,j+1} - u_{0,j}}{x_{j+1} - x_j}. \tag{40}$$

This field is used to perform a time step to update the value of the magnetization, see (31).

We implemented this scheme to solve (31) using the optimal grid with $n = 6$ and $\kappa = 4 \times 10^4$, scaled to have $h_0 = h_\perp$. As in the previous section, we used $x_{j+1/2} = b \sinh[h_\perp(j - m/2)/b]$. Note that with this choice of the optimal grid parameters the accuracy of the approximation of the square root coincides with that of the optimal geometric grid, on essentially the same spectral interval. Not surprisingly, the results of the simulations agreed with those of Section 4.1, with the same convergence properties as in Fig. 3. In fact, the same accuracy could be achieved, for example, with $h_\perp = 0.25$, using only $n = 4$ and $\kappa = 10^4$ (essentially, the scaled version of the grid shown in Table 1).

To further investigate the performance of these methods, we ran well-resolved simulations of (31) and compared the run times. In all the runs we chose $h_\perp = 0.05$ and large enough domain to obtain the energy and other parameters of the Neél wall to within at least three significant digits. The optimal geometric and Zolotarev grids were constructed as explained above, except the Zolotarev grid was based on the optimal rational approximation of the square root on the interval with $\kappa = 10^6$. Both the optimal geometric and the Zolotarev grid-based codes used non-uniform grids in x as explained above with $b = 0.9$, and the same convergence criterion was used for the CG iterations. The size of the obtained optimal grids is given by L_z, and the domain size is given by L_x (see Tables 2 and 3).

We compared these results to the ones obtained by the FFT-based (cosine transform and pseudospectral) methods. Both the cosine transform and the pseudospectral codes used the same explicit time-stepper as for the optimal grid simulations (with the same time step $\Delta t = 0.001$). These results are also compared with the "exact" results obtained using the same pseudospectral algorithm which uses fourth-order Runge–Kutta method in time with an integrating factor for diffusion to improve stability of the algorithm (here we used $h_\perp = 0.25$ and $\Delta t = 0.025$) and a sufficiently large domain to obtain the solution up to at least 6 significant digits. Of course, as far as high accuracy is concerned, pseudospectral method is superior in this particular problem, since it requires fewer discretization points due to exponentially small truncation error. Nevertheless, for a fair comparison of the methods, we did pseudospectral runs with the same number of nodes as in the cosine transform method.

The results of these runs, starting with the initial data $\theta(x) = \pi/(1 + e^{x/2})$, can be summarized in Tables 2 and 3. Table 2 shows the run times, the values of the wall energy, and the maximum value of the stray field,

Table 2

Method	T (s)	n	m	L_x	L_z	E	$h(0)$
Geometric grid	19.2	10	256	1102.95	303.29	2.219161	0.360774
Optimal grid	5.0	6	257	1102.95	258.25	2.219856	0.359566
Cosine transform	30.1	1	16,384	819.20	0	2.218795	0.360798
Pseudospectral	54.0	1	16,384	819.20	0	2.218908	0.360812
"Exact"	7.3	1	16,384	4096	0	2.218915	0.360823

Table 3

Method	T (s)	n	m	L_x	L_z	E	$h(0)$
Geometric grid	29.6	10	256	1102.95	303.29	2.213443	0.381807
Optimal grid	11.6	6	257	1102.95	258.25	2.214215	0.381801
Cosine transform	302	1	16,384	819.20	0	2.213056	0.381766
Pseudospectral	510	1	16,384	819.20	0	2.213160	0.381816
"Exact"	78.8	1	16,384	4096	0	2.213164	0.381820

obtained from these simulations at $t = 2.5$. The runs were performed on a 1.33 GHz Macintosh PowerBook G4 computer. The first thing to observe is an almost 4-fold speedup when using the Zolotarev optimal grid, as compared to the optimal geometric grid. The speedup is partly due to fewer number of nodes in the z-direction, and also due to fewer number of iterations of the CG method needed to achieve the same accuracy when solving the discrete boundary value problem for u. Secondly, both methods beat the cosine transform method, which is quite impressive in view of the fact that the latter is usually the method of choice for the considered class of problems. This is because the optimal grid methods use vastly fewer nodes, only where they are needed to resolve the fine structure of the solution. The pseudospectral method did worse still because of the need to perform more FFTs.

This difference becomes even more dramatic in the second series of runs summarized in Table 3. Here, the same quantities are shown, but now at $t = 25$. The evolution of θ for $2.5 < t < 25$ is a slow relaxation towards the domain wall solution. Now the optimal grid codes beat the cosine transform code by a factor of over 10, and the Zolotarev grid code beats it by a factor of 30. This is due to the fact that when the evolution becomes slow, it only takes a few (often just one) CG iterations during each time step for it to converge. This is an extra advantage of an iterative optimal grid-based method for evolution equations involving non-local operators, as it uses less time during slow phase of the dynamics.

To demonstrate the true multiscale nature of the method, we computed the solution in the form of the Neél wall in a soft material like permalloy. We chose $v = 250$, which for the parameters of permalloy discussed in Section 2 corresponds to a 20 nm-thick film. Here, we set $h_\perp = 0.02$, $b = 0.4$ and used $m = 513$ nodes to achieve a grid whose extent in x is $L_x \simeq 1.5 \times 10^5$. To generate a comparable grid in z, we constructed an optimal approximation to the square root with $n = 8$ on a spectral interval with $\kappa = 10^{12}$. Choosing $h_0 = h_\perp$, we find that the "length" of the optimal grid in the z-direction is $L_z = 5.5 \times 10^4$, and the relative error of this optimal approximant is within about 2%. The obtained solution in the form of the Neél wall is presented in Fig. 5. The two characteristic features of the Neél walls: the logarithmic tail followed by the algebraic decay [21], can all be clearly seen from these data, replotted in logarithmic scale in Fig. 6.

4.3. Two-dimensional simulations

In this section, we extend the approach of Section 4.2 to two-dimensional films. Here, we consider a finite rectangular sample in free space, and, hence, need also to take into account boundary effects. This, however, is easily done by combining the optimal grids in both x, y- and z-directions [34]. This is illustrated in Fig. 7. Similarly to the one-dimensional case, the material is broken up into square cells, and the magnetization is represented by the grid points in the centers of these cells (squares). The potential nodes (circles) are placed at the vertices of the material cells. The xy-grid is then extended into free space by using the steps of the optimal grid in one (either x or y) or both directions in the xy-plane. The full three-dimensional grid is then taken to be a Cartesian product of the xy-plane grid just described and the optimal grid in z [34].

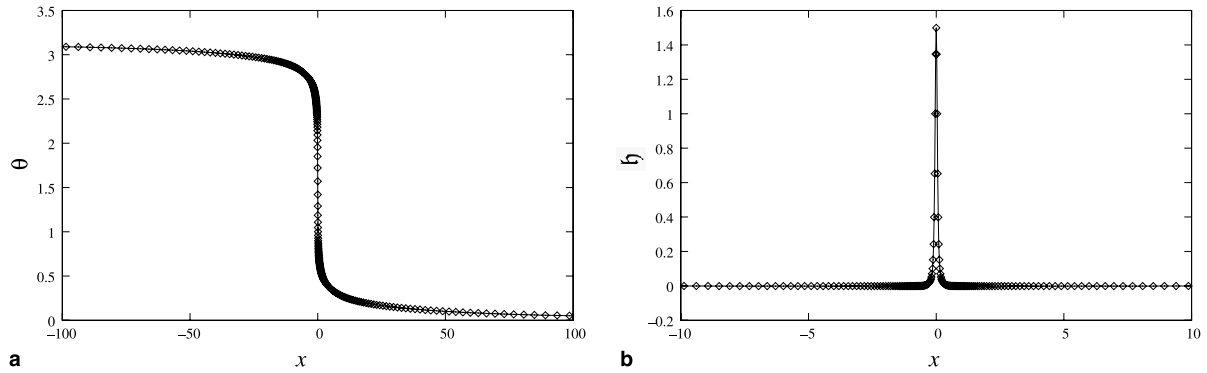

Fig. 5. The profile of the Neél wall at $v = 250$ obtained using Zolotarev optimal grid. Results of the numerical solution of (31) with $h_\perp = 0.02$, $h_0 = h_\perp$, $\kappa = 10^{12}$, $n = 8$, $m = 513$, $b = 0.4$. (a) The angle variable θ. (b) The stray field h.

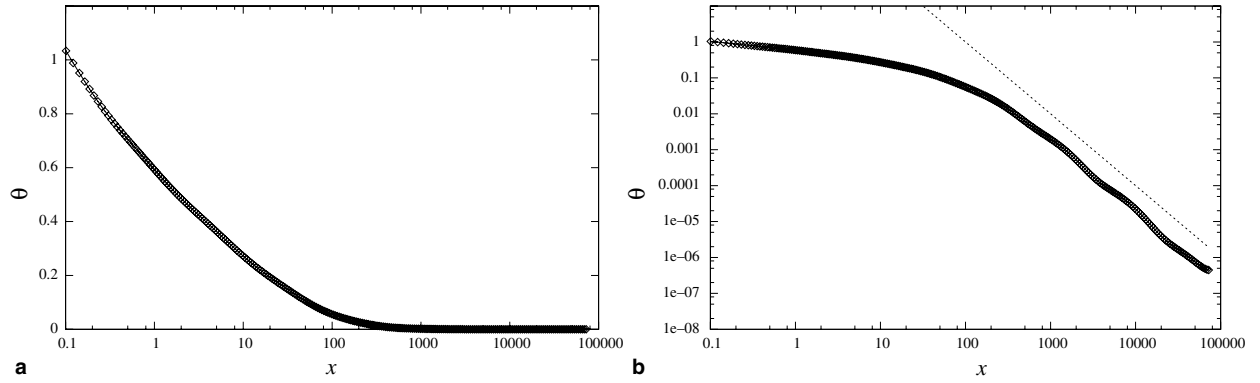

Fig. 6. The tail of the Neél wall at $v = 250$ obtained in the simulation of Fig. 5, replotted in log-linear (a) and log-log (b) scales. In (b), the dotted line shows algebraic decay $\sim 1/x^2$.

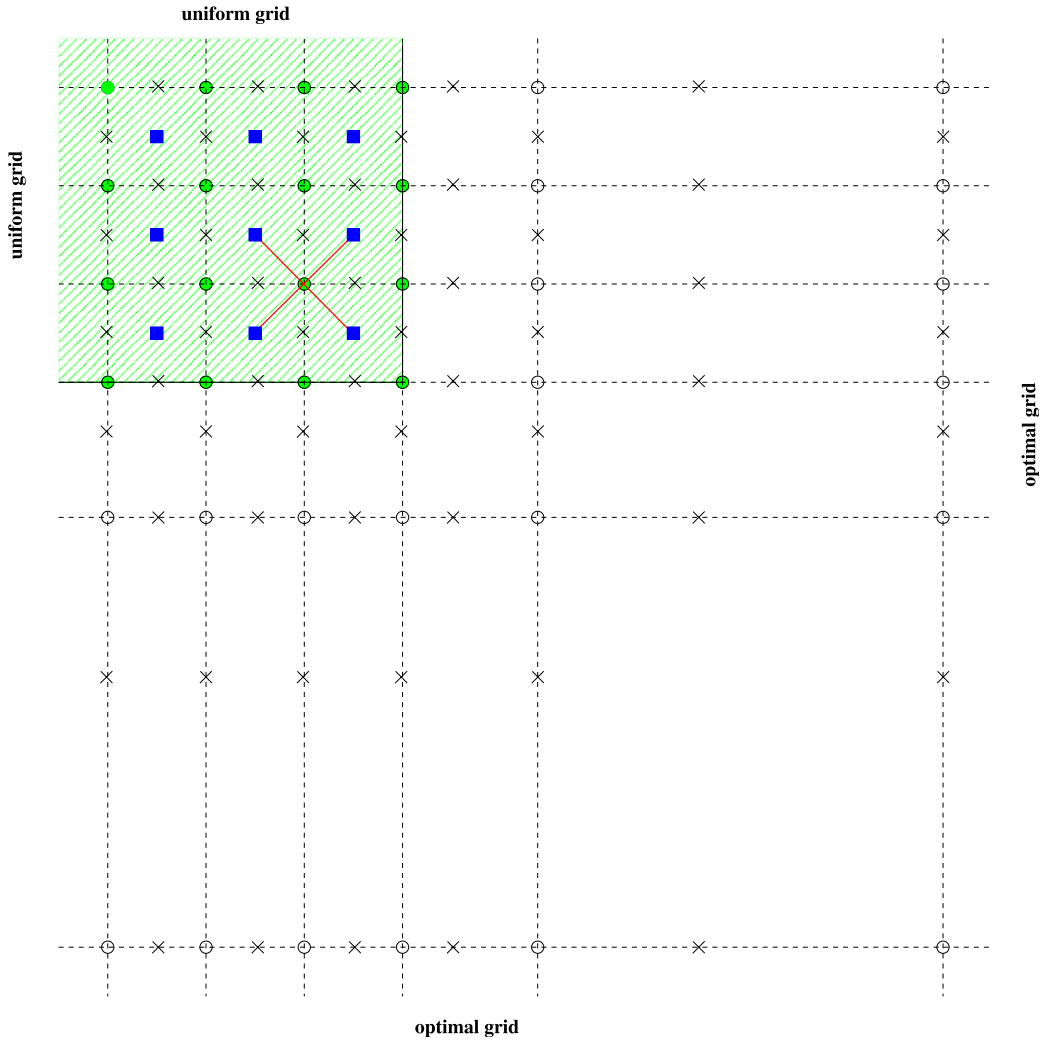

Fig. 7. The schematics of the in-plane discretization for two-dimensional rectangular film. The circles (○) show potential nodes, the crosses (×) the derivative nodes, the squares (□) the magnetization nodes, and the filled circles (●) the charge nodes. The shaded region shows the magnetic film.

The solution is then computed as follows. First, the magnetic charges at the potential nodes are computed by approximating $-\nabla \cdot \mathbf{m}$ obtained from θ, using a pair of centered differences along the diagonals of the cells (two thin lines in Fig. 7 for a representative node). To account for the boundary of the material, we assume that $\mathbf{m} = 0$ in the fictitious cells immediately outside the film, this generates surface charges at the film boundary. Once the charges are obtained, the problem for the potential u is solved using CG as before, and then the gradient of the potential is computed, again, using centered differences in the directions of the diagonals of the square. The field, in turn, is used to do a time step to evolve θ.

We performed a series of fully resolved simulations and recovered a number of well-known domain structures [1], which further corroborates the validity of our method. First, we considered a sample that is elongated in the direction of the easy axis, and set $\nu = 10$ to make the effect of the stray field more significant (this would correspond, e.g., to an ultra-thin 2 nm-thick permalloy film for the parameters of [29]). We discretized the film on a 33×65 uniform grid and used a Zolotarev optimal grid with $n = 6$ nodes and $h_0 = h_\perp = 0.25$, optimized for $\kappa = 2.5 \times 10^5$ (this gives the relative error on the spectral interval within 0.2%, with $L_z \simeq 770$). From the initial condition with all the magnetization vectors at a 45° angle to the easy access, the attained steady-state is shown as a vector field in Fig. 8. This configuration is the well-known S-state. Because of the rather large value of ν, magnetostatic energy gets strongly penalized, and so the vector of magnetization

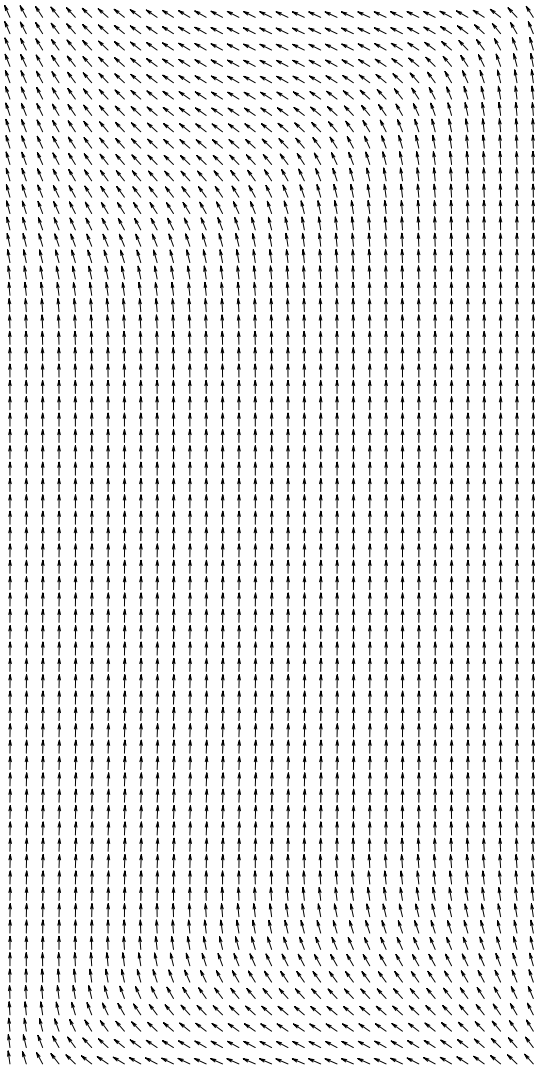

Fig. 8. The S-state obtained in the simulation with $\nu = 10$, $m_x = 33$, $m_y = 65$, $n = 6$, $\kappa = 2.5 \times 10^5$, $h_0 = h_\perp = 0.25$.

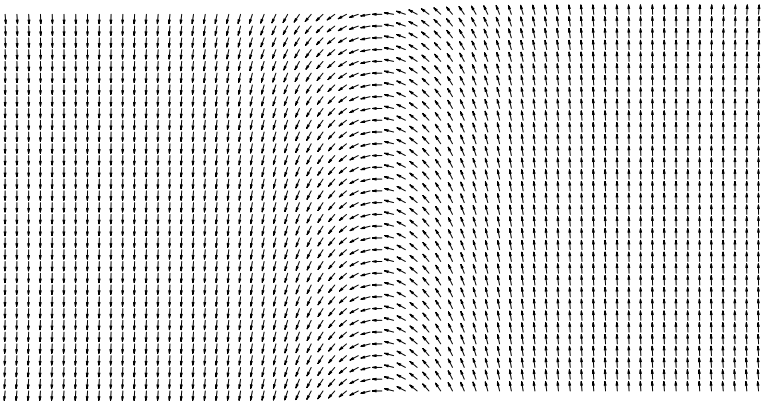

Fig. 9. The Neél wall in a finite rectangular sample. Results of the simulations with $v = 1$, $m_x = 65$, $m_y = 33$, $n = 6$, $\kappa = 2.5 \times 10^5$, $h_0 = h_\perp = 0.25$.

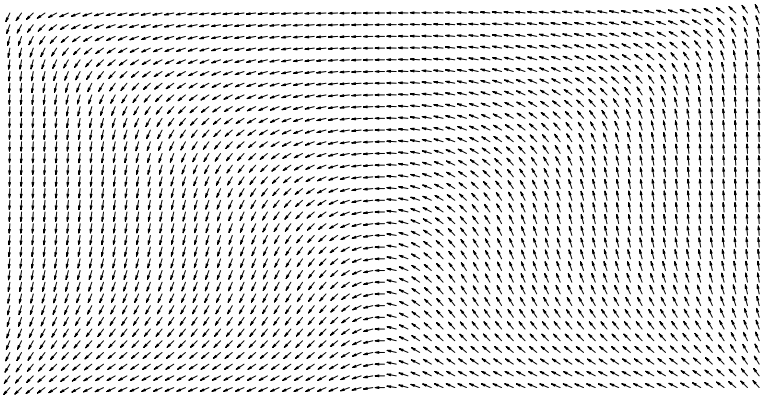

Fig. 10. The C-state obtained in the simulation with $v = 10$, $m_x = 65$, $m_y = 33$, $n = 6$, $\kappa = 2.5 \times 10^5$, $h_0 = h_\perp = 0.25$.

tries to align normally to the film top and bottom edges. This results in the formation of excess charges in the top-left and bottom-right corners of the film.

We next examine the effect of the boundaries in finite rectangular films on the one-dimensional Neél walls. Here, we consider the samples that are elongated in the direction perpendicular to the easy axis. We first choose $v = 1$ and other parameters as above, except the film is 65×33 cells. The apparent steady-state obtained from the initial data in the form of a one-dimensional Neél wall-like profile is shown in Fig. 9. One can see that the domain wall is not significantly affected by the boundaries for this value of v.

On the other hand, one can see a change in behavior at larger values of v. We repeated the preceding simulation at $v = 10$, the obtained steady-state is shown in Fig. 10. In this case the charges on the top and bottom edges of the sample are strongly penalized, and so the magnetization vector tends to align parallel to the boundaries, creating a pair of opposite charges at the bottom right and left corners, and the remnants of the Neél wall structure in the mid-bottom part of the sample. This is essentially a C-state.

We would like to point out that these runs are very fast and take on the order of only a minute to execute on the same computer as before. In fact, simulations of films discretized to 500×500 nodes can be routinely handled by this method.

5. Conclusion

To summarize, we have presented a new method for computing the stray field in the thin film micromagnetics simulations based on the LLG equation. The method takes advantage of the recently proposed idea of

optimal grids for approximating the Neumann-to-Dirichlet map associated with the Laplace's equation in free space, and relies on the optimal rational approximation of the square root of the in-plane Laplacian in operator sense.

We have demonstrated the efficiency and ease of use of this method as compared to the more conventional FFT-based approaches in the case of a reduced model of ultra-thin film micromagnetics. The chief advantage of our approach is the fact that it uses a conservative finite difference discretization of the free space problem, which admits the use of non-uniform grids in the film plane, while requiring vastly fewer discretization nodes in the direction normal to the film surface. This opens up a possibility to combine the optimal grid discretization in the normal direction with an adaptive in-plane discretization, which is needed to resolve fine magnetic structures forming in these materials, for a truly multiscale approach to thin film micromagnetic simulations.

We also demonstrated that a combination of optimal grids in all directions can be used to efficiently treat the boundary charges forming on the film edges in a finite sample, with essentially no extra cost for solving the exterior problem. Similarly, our approach is not limited to only infinitesimally thin magnetic films and can be used to study films of finite thickness by simply adding more material layers in the normal direction and gluing together a uniform grid, say, for the bulk of the material with an optimal grid in the free space. Naturally, the method is also not limited to film geometries and can be extended in a variety of ways. This, together with a straightforward parallelization, may provide a very powerful computational tool for studying three-dimensional magnetic structures in micromagnetics and can become useful for the development of new magnetic devices.

Acknowledgements

The authors acknowledge multiple valuable discussions with V. Druskin. The work of CBM was partially supported by NSF via Grant DMS02-11864, and NIH via Grant R01 GM076690.

References

[1] A. Hubert, R. Schäfer, Magnetic Domains, Springer, Berlin, 1998.
[2] A. Aharoni, Introduction to the Theory of Ferromagnetism, Oxford University Press, New York, 1998.
[3] S.V. Vonsovskii, Ferromagnetism, Wiley, New York, 1974.
[4] R. Jansen, M. Speckmann, H.P. Oepen, H. van Kempen, Morphology and magnetism of thin Co films on textured Au surfaces, J. Magn. Magn. Mater. 165 (1997) 258–261.
[5] M. Speckmann, H.P. Oepen, H. Ibach, Magnetic domain-structures in ultrathin Co/Au(1 1 1) – on the influence of film morphology, Phys. Rev. Lett. 75 (1995) 2035–2038.
[6] R. Allenspach, A. Bischof, Magnetization direction switching in Fe/Cu(1 0 0) epitaxial-films – temperature and thickness dependence, Phys. Rev. Lett. 69 (1992) 3385–3388.
[7] A. Berger, H.P. Oepen, Magnetic domain walls in ultrathin fcc cobal films, Phys. Rev. B 45 (1992) 12596–12599.
[8] R. Allenspach, M. Stampanoni, A. Bischof, Magnetic domains in thin epitaxial Co/Au(1 1 1) films, Phys. Rev. Lett. 65 (1990) 3344–3347.
[9] B. Heinrich, J.A.C. Bland (Eds.), Ultrathin Magnetic Structures, Springer, Berlin, 1994.
[10] T. Miyazaki, N. Tezuka, Giant magnetic tunneling effect in Fe/Al_2O_3/Fe junction, J. Magn. Magn. Mater. 139 (1995) L231–L234.
[11] J.S. Moodera, L.R. Kinder, T.M. Wong, R. Mesrevey, Large magnetoresistance at room-temperature in ferromagnetic thin-film tunnel-junctions, Phys. Rev. Lett. 74 (1995) 3273–3276.
[12] W.H. Rippard, R.A. Buhrman, Ballistic electron magnetic microscopy studies of magnetization reversal in Co/Cu/Co trilayer films, J. Appl. Phys. 87 (2000) 6490–6492.
[13] Proceedings of International Conference on Magnetism, Elsevier, Recife, Brasil, 2000.
[14] E.B. Meyers, D.C. Ralph, J.A. Katine, R.N. Louie, R.A. Buhrman, Current-induced switching of domains in magnetic multilayer devices, Science 285 (1999) 867–870.
[15] M. Tsoi, A.G.M. Jansen, J. Bass, W.-C. Chiang, M. Seck, V. Tsoi, P. Wyder, Excitation of a magnetic multilayer by an electric current, Phys. Rev. Lett. 80 (1998) 4281–4284.
[16] J.A. Katine, F.J. Albert, R.A. Buhrman, E.B. Meyers, D.C. Ralph, Current-driven magnetization reversal and spin-wave excitations in Co/Cu/Co pillars, Phys. Rev. Lett. 84 (2000) 3149–3152.
[17] A. DeSimone, R.V. Kohn, S. Müller, F. Otto, Magnetic microstructures – a paradigm of multiscale problems, in: ICIAM 99 (Edinburgh), Oxford University Press, Oxford, 2000, pp. 175–190.
[18] G. Gioia, R.D. James, Micromagnetics of very thin films, Proc. Roy. Soc. Lond. Ser. A 453 (1997) 213–223.
[19] C.J. Garcia-Cervera, W. E, Effective dynamics for ferromagnetic thin films, J. Appl. Phys. 90 (2001) 370–374.
[20] A. Desimone, R.V. Kohn, S. Müller, F. Otto, A reduced theory for thin-film micromagnetics, Commun. Pure Appl. Math. 55 (2002) 1408–1460.

[21] C.J. Garcia-Cervera, One-dimensional magnetic domain walls, Euro. J. Appl. Math. 15 (2004) 451–486.
[22] A. DeSimone, H. Knüpfer, F. Otto, 2-D stability of the néel wall, Tech. rep., SFB, 2004.
[23] R.V. Kohn, V. Slastikov, Effective dynamics for ferromagnetic thin films: a rigorous justification, Proc. Roy. Soc. Lond. Ser. A 461 (2005) 143–154.
[24] J. Fidler, T. Schrefl, Micromagnetic modelling – the current state of the art, J. Phys. D 33 (2000) R135–R156.
[25] S.W. Yuan, H.N. Bertram, Fast adaptive algorithms for micromagnetics, IEEE Trans. Magn. 28 (1992) 2031–2036.
[26] W. Scholz, J. Fidler, T. Schrefl, D. Suess, R. Dittrich, H. Forster, V. Tsiantos, Scalable parallel micromagnetic solvers for magnetic nanostructures, Comput. Mater. Sci. 28 (2003) 366–383.
[27] T. Trunk, M. Redjdal, A. Kákay, M.F. Ruane, F.B. Hunphrey, Domain wall structure in permalloy films with decreasing thickness at the Bloch to Néel transition, J. Appl. Phys. 89 (2001) 7606–7608.
[28] C.J. Garcia-Cervera, Z. Gimbutas, W. E, Accurate numerical methods for micromagnetics simulations with general geometries, J. Comput. Phys. 84 (2003) 37–52.
[29] NIST Micromagnetic Modeling Activity Group. URL: http://www.ctcms.nist.gov/~rdm/mumag.html.
[30] X.P. Wang, C.J. Garcia-Cervera, W. E, A Gauss–Seidel projection method for the Landau–Lifshitz equation, J. Comput. Phys. 171 (2001) 357–372.
[31] S.V. Tsynkov, Numerical solution of problems on unbounded domains. A review, Appl. Numer. Math. 27 (1998) 465–532.
[32] V. Druskin, Spectrally optimal finite difference grids in unbounded domains, Schlumberger-Doll Research Notes (1997) EMG-002-97-22.
[33] D. Ingerman, V. Druskin, L. Knizhnerman, Optimal finite difference grids and rational approximations of the square root: I. Elliptic problems, Commun. Pure Appl. Math. 53 (2000) 1039–1066.
[34] V. Druskin, S. Moscow, Three-point finite difference schemes, Padé and the spectral Galerkin method. I. One-sided impedance approximation, Math. Comput. 71 (2001) 995–1019.
[35] B. Heinrich, J.F. Cochran, Ultrathin metallic magnetic films: magnetic anisotropies and exchange interactions, Adv. Phys. 42 (1993) 523–639.
[36] M.E. Taylor, Partial Differential Equations II: Qualitative Studies of Linear Equations, Springer, Berlin, 1996.
[37] P. Petrushev, V.A. Popov, Rational approximation of real functionsEncyclopedia of Mathematics and Its Applications, vol. 28, Cambridge University Press, Cambridge, 1987.
[38] E.W. Cheney, Introduction to Approximation Theory, second ed., AMS, Providence, RI, 1999.
[39] G.A. Baker, P. Graves-Morris, Padé Approximants, second ed.Encyclopedia of Mathematics and Its Applications, vol. 59, Cambridge University Press, Cambridge, 1996.